Multi-exposure adaptive threshold technique for cloud detection with sky imagers

A. Cazorla [a,b,*], C. Husillos [c], M. Antón [d], L. Alados-Arboledas [a,b]

[a] *Instituto Interuniversitario del Sistema Tierra en Andalucía, Avda. del Mediterraneo s/n, 18006 Granada, Spain*
[b] *Departmento de Física Aplicada, Universidad de Granada, Avda. Fuentenueva s/n, 18071 Granada, Spain*
[c] *Instituto de Astrofísica de Andalucía, Glorieta de la Astronomía s/n, 18008 Granada, Spain*
[d] *Departmento de Física, Universidad de Extremadura, Avda. de Elvas s/n, 06071 Badajoz, Spain*

Abstract

Sky imagers have been used for cloud detection and classification in the last years, and one of the applications of these instruments is the use of cloud information in forecast algorithms for solar power technologies. These algorithms depend on an accurate classification of the complete sky dome cloud cover, but most system fail in the proximity of the sun due to saturation in the images. This work proposes a new method for cloud detection with sky imagers using images taken with different exposure times and applying an adaptive threshold to each one. The use of multiple exposure times avoids the saturation of the image in the vicinity of the sun position, while the adaptive threshold applied to the images helps in the accurate detection of cloud coverage, especially in the circumsolar area. The method is tested with a commercial sky imager, paying special attention to the detection of clouds close to the sun position. A case study is analyzed, showing an accurate detection of clouds in the vicinity of the sun. The method is also validated using statistical values for data recorded during almost one month which cover a great variety of cloudiness cases. For this purpose, the detection of clouds in the sun position is compared against the reduction of the direct normal irradiance (DNI) with respect to a modeled DNI.
© 2015 Elsevier Ltd. All rights reserved.

1. Introduction

The characterization and forecast of the solar resource in renewable energy systems is essential for the planning and optimization of the electricity production in solar power plants (Eck and Hirsch, 2007; Sharma et al., 2009; Medrano et al., 2010). Accurate forecast of the available solar irradiance reaching the ground allows solar power plant operators to predict the energy output of the plant,

anticipate the storage needs and regulate the system. For large scale solar applications, the solar irradiance at the surface is affected mainly by aerosols, water vapor content and clouds, being the last the most variable in time and space. Photovoltaic (PV) plants depend on the Global Horizontal Irradiance (GHI) availability, whereas concentration solar power (CSP) plants and concentration photovoltaic systems (CPV), rely on the availability of direct normal irradiance (DNI) reaching the collectors.

It is well known that the solar radiation may exhibit a strong variability at very short-time scales related mainly to cloud changes (e.g., Tovar et al., 1998; 1999; Tomson and Tamm, 2006; Woyte et al., 2007; Tomson, 2010;

---

* Corresponding author at: Avda. del Mediterraneo s/n 18006 Granada, Spain. Tel.: +34 958249751.

E-mail address: cazorla@ugr.es (A. Cazorla).

Antón et al., 2011). Thus, for intra-hour prediction of the available solar irradiance is essential to introduce in the models information about the cloud cover. This is especially important in the case of CSP and CPV, where the presence of clouds obstructing the solar disk reduces the amount of available DNI drastically.

Recently, Ahmad and Tiwari (2011) made a review of solar radiation models. Some of the early models taking into account the effect of the cloud included information about the cloud coverage, whereas more recent ones take into account the cloud type, the location of the cloud in relation to the sun's position, and the total cloud coverage that affects diffuse irradiance (e.g. Hammer et al., 2003).

Sky imagers are potentially helpful for developing short-term solar irradiance prediction by means of forecasting models. Thus, Crispim et al. (2008) included cloud features extracted from a Total Sky Imager (TSI) in a forecast model with 60 min ahead horizon. Marquez et al. (2013) used cloud indices from the TSI built-in algorithms, and cloud indices derived from Infrared Radiometric (IR) measurements in a model for 60 min ahead horizon forecasting of Global Horizontal Irradiance (GHI). Chow et al. (2011) proposed a model for GHI forecasting projecting the cloud field extracted from TSI images several minutes ahead, concluding that the methodology with the TSI was useful for horizons up to 15–20 min. Marquez and Coimbra (2013) also proposed a method that uses the cloud cover provided by a TSI for a time series forecasting of DNI up to 15 min ahead horizon.

The forecast of solar irradiance using sky imagers critically depends on an accurate detection of clouds by these instruments. The algorithm most widely used to provide the estimation of the cloud cover in sky imagers is the red-to-blue ratio (RBR) threshold algorithm or a variation of it. This algorithm was introduced by Johnson et al. (1989) and Shields et al. (1998) and consists in applying a threshold to the result of dividing the red and blue channel of the images. The idea behind this algorithm is that the sky appears blue to our eyes, whereas clouds appear white or grey. Thus, for a cloudy pixel the result of dividing the red and blue channels will be a number close to one, whereas for a clear-sky pixel the result will be a smaller number. Applying an appropriate threshold, the result is a binary image that represents cloudy pixels (above the threshold) and clear-sky pixels (below the threshold). The value of this threshold must be determined empirically since it depends on the sensor and the atmospheric conditions, complicating the selection of an optimum threshold that works in every situation. Moreover, the images capture the entire sky dome, thus the angular dependence of the light scattering processes makes difficult to find an optimum threshold that works across the entire image (Pfister et al., 2003). Another problem that introduces errors in the estimation of cloud cover is the saturation of pixels due to forward scattering in the circumsolar area. Images projecting the entire sky dome have very bright areas where the sun is projected, several order of magnitude brighter than darker regions

of the sky dome. Sky imager sensors are not able to cover such a range illumination causing that some pixels of the image reach the maximum intensity (saturation). When pixels are saturated it is impossible to determine if the pixels represented clear-sky or cloudy areas. In the RBR threshold algorithm, saturated pixels are always classified as cloudy pixels. The extension of the circumsolar saturated area varies with the aerosol load (the higher the load the more forward scattering and, therefore, more brightness around the sun). This is especially evident for large solar zenithal angles (during sunrise and sunset) when the direct sun irradiance has a longer path throughout the atmospheric boundary layer (Chow et al., 2011; Long et al., 2006; Pfister et al., 2003).

A review of different methods for cloud detection and classification can be found in Tapakis and Charalambides (2013). Some of the authors referenced presented different approaches in order to minimize the misclassifications in sky images. Cazorla et al. (2008) described a classification method using artificial neural networks. Shields et al. (2009) proposed a clear-sky library that is subtracted to the image after applying the RBR algorithm to minimize the angular dependency of the threshold. This idea was also applied to a Total Sky Imager by Ghonima et al. (2012). Calbó and Sabburg (2008) explored the idea of using feature extraction from the images for cloud type classification.

Other authors used a different color space (Souza-Echer et al., 2006). Pfister et al. (2003) and Long (2010) proposed statistical analysis of a sequence of images. Kazantzidis et al. (2012) proposed a multicolor criterion for cloud detection and classification. Recently, Urquhart et al. (2014) described a new sky imager with high dynamic range capabilities.

In this work, we present a new method for cloud detection with sky imagers using images taken with different exposure times and applying an adaptive threshold to each one. This new method helps in the accurate prediction of cloud coverage, especially in the circumsolar area. The method is illustrated with a study case and validated using images acquired under a great variety of cloudy conditions throughout one month.

2. Site and instrumentation

The instrumentation used in this work is operated by the Atmospheric Physics Group (GFAT) at University of Granada. The station is located at Granada in the rooftop of the Andalusian Institute for Earth System Research (IISTA-CEAMA) (37.17°N, 3.61°W, 680 m a.s.l.). Granada, located in south-eastern Spain, is a non-industrialized city with about 250,000 inhabitants (500,000 including the metropolitan area). It is located in a natural basin surrounded by mountains with elevations between 1000 and 3500 m a.s.l. The near-continental conditions prevailing at this site are responsible for large seasonal temperature differences, providing cool winters and hot summers. The

bowl-like topography of the Granada basin favors wintertime thermal inversions and the predominance of very low wind speeds (Lyamani et al., 2010).

The sky imager used in this work is the SONA (Sistema de Observación de Nubosidad Automático, Automatic Cloudiness Detection System) developed by Sieltec Canarias S.L (González et al., 2012). The system consists of a color CCD sensor with a resolution of 640 × 480 pixels. RGB images have 8 bit-digitalization yielding 256 counts per channel. The system is programmable allowing the change of time exposure needed for the algorithm described in the following sections. The sensor is coupled with a fisheye lens that projects the entire sky dome in the sensor. CCD sensor and lens are encapsulated in an environmental housing with a glass dome on top. The sensor is protected from the direct sun light with a shadow band that is also inside the glass dome and isolated from the environment.

The station is equipped with two pyranometers (CM-11, Kipp & Zonen), one of them provides measurements of the global solar horizontal irradiance from 0.305 to 2.800 μm and the other one, mounted on a solar tracking platform with a shade ball (2AP Sun Tracker, Kipp & Zonen), measures the diffuse solar horizontal irradiance (DIF). The CM-11 pyranometer is fully compliant with the highest ISO performance criteria for this type of instruments. The relative uncertainty of these pyranometers is estimated to be 1.9% (Kratzenberg et al., 2006). The stability of the two pyranometers has been periodically verified using a reference CM-11 instrument located at the station and used only for intercomparison purposes, and traceable with reference instruments form the World Radiation Center (WRC) placed at Davos (Switzerland). Measurements are recorded every minute using a single data-logger (CR10-X, Campbell Scientific).

3. Methodology

The technique proposed in this work tries to solve the problems related to sky imagers and their detection algorithms by, firstly registering the images at several exposure times (solving the lack of dynamic range that cause saturation of the circumsolar area) and, secondly, applying a threshold that depends on the amount of light captured by the sensor and the distance of a given pixel to the sun.

3.1. Multi-exposure sequence

The exposure time in photography is the amount of time that the sensor is exposed to the light. Most sky imagers have an algorithm that analyzes the illuminance of the scene and selects an appropriate exposure time for the image, or uses fixed exposure times. Nevertheless, if the differences in illumination are larger than the range of the sensor, i.e. the sensor does not have enough dynamic range to represent the scene, some parts of the image will be overexposed, or saturated (reaching the maximum counts of the sensor), and some others will be underexposed. Fig. 1 shows a sky

image captured with the SONA sky imager. We observe that there are saturated pixels around the sun position (yellow circle over the shadow band). A very short exposure time will produce a correct exposure of the area around the sun, but the rest will be underexposed. In contrast, a longer exposure time will cause an overexposure of the area around the sun (this region will be saturated) in order to get the rest of the image well exposed. The multi-exposure algorithm takes images with several exposure times ranging from very short to longer exposure times. SONA sky imager captures 12 images starting from the minimum exposure time available (0.004 ms) and doubling it in each image up to an exposure time of 8 ms. Some of these images can be discarded if they are too dark or too bright depending on both the sky conditions and sun position. Fig. 2 shows a sequence of multi-exposure images in which pixels close to saturation are marked in red while dark pixels are marked in green. The horizon, the shadow band and other objects are masked in black. As it can be seen, the unmasked area in the images is well exposed and, by visual inspection, it is feasible to discriminate better the cloudy and cloudless areas than using the image shown in Fig. 1.

All images from the multi-exposure sequence are captured in about 5 s. These images can be merged into one single image that combines information from the well exposed areas of each individual image to form a high dynamic range image (HDR, Debevec and Malik, 1997). For visualization purposes, we combine all the images into an HDR composite (Fig. 3) by averaging the non-saturated pixels of the different images in the multi-exposure sequence. It must be pointed out that this image has an appearance more similar to what our eyes can see compared to the image in Fig. 1, however, for the detection algorithm, each individual image from the sequence is used.

The next step is to find a threshold that separate cloudy and cloudless areas from the images captured with the multi-exposure sequence as will be described in the next section.
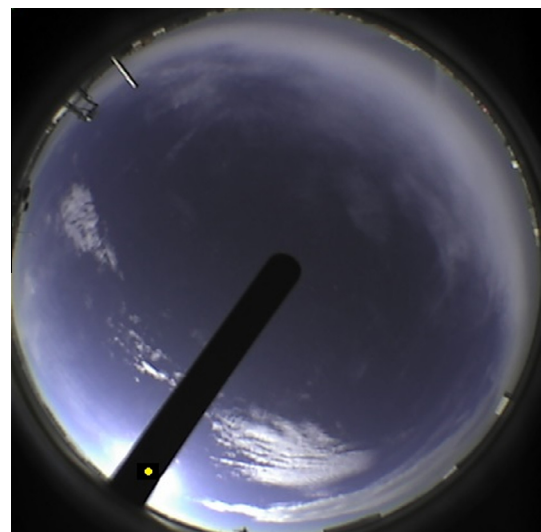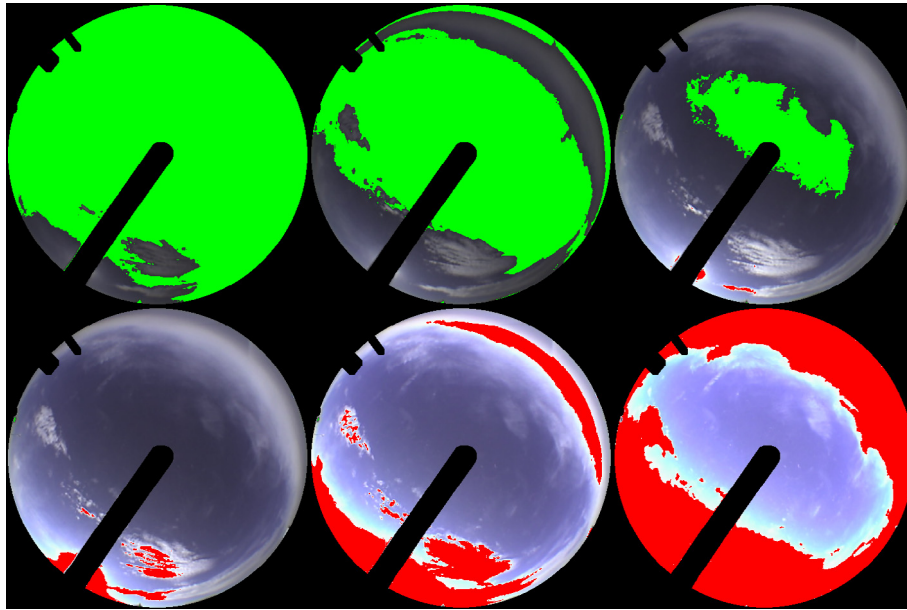

Fig. 1. Sky image capture by the SONA sky imager.

Fig. 2. Sequence of multi-exposure images captures with the SONA sky imager. Underexposed areas of the image (*B* counts bellow 85) are marked in green and overexposed (*B* counts above 240) are marked in red. (For interpretation of the references to color in this figure legend, the reader is referred to the web version of this article.)
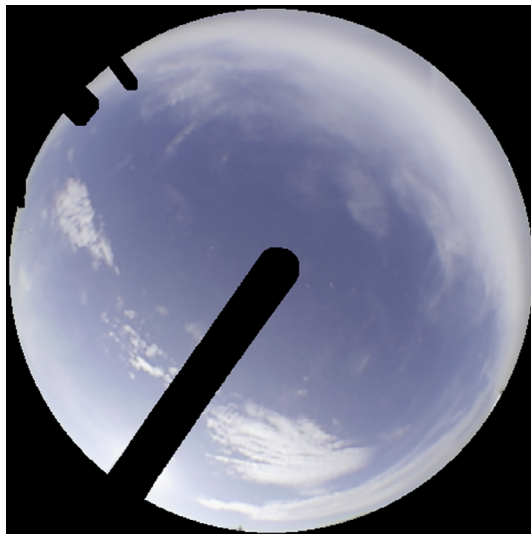

Fig. 3. High dynamic range composite using a sequence of multi-exposure images.

Fig. 4. Red-to-blue ratio (RBR) vs. blue (*B*) counts plot for clear-sky (blue) and cloudy (red) pixels. (For interpretation of the references to color in this figure legend, the reader is referred to the web version of this article.)

3.2. The adaptive threshold

The first step is to obtain the RBR images for the sequence of multi-exposure images by dividing the R and B channels of each image. The sky imager used in this work applies a white balance (i.e. a color gain) with values of 1.46 for the R channel and 1.66 for the B channel, and a gamma correction of 1.4 in order to appear more realistic. These have an impact on the relationship between the red and blue channel. In order to parameterize this dependency, for the image sequence shown in Fig. 2, pixels are randomly selected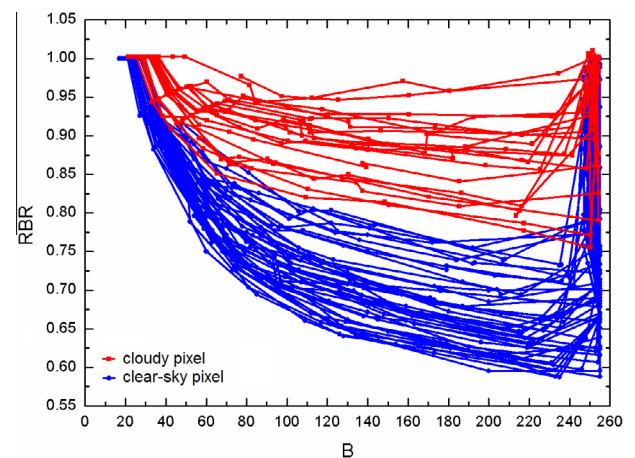 and manually classified as clear-sky or cloudy. For these pixels, Fig. 4 shows the relationship between RBR values and *B* counts for the different exposure times of the image sequence. Each curve represents a pixel and each data point in the curve corresponds to an exposure time. The *B* counts increase with increasing exposure time, while the RBR decreases systematically for all cases (clear-sky and cloudy). This indicates that the blue channel increases at a higher rate than the red channel as the exposure time increases, i.e. the sensitivity of the channels is different. This behavior changes drastically when the *B* counts are close to saturation (255). We also observe that this dependency is almost linear if we focus our attention in a specific range of counts (85–240 counts). The selection of

this range is decided based on the R-square of the linear fit. For all the pixels used, we calculate the linear fit and the R-square using the full range and then, iteratively we reduce the interval, firstly reducing by one on the upper limit of the interval until there is a sudden change. On average, 240 is the number of counts where the descending behavior ends. Then, succeeding the fixing of the upper limit of the interval, we iterate on the lower limit until the R-square is greater than 0.95. On average, for the pixel analyzed, the lower limit is 85. Finally, we can fit the RBR values as a function of the B counts (in the range 85–240 B counts) following the equation

$$RBR = T_s * B + T_i \qquad (1)$$

where T_s and T_i are the slope and the intercept of the linear fit respectively.

Fig. 4 also shows a separation of pixels representing clear-sky and clouds. However, it can be seen that the use of a fixed RBR threshold can be problematic in separating clear-sky and cloudy pixels, especially when the B counts are low. Also the spread of the data, particularly for clear-sky pixels can be explained by the angular distance between the sun and the corresponding pixel in the sky dome. In order to illustrate this dependency, several clear-sky image sequences acquired at different sun elevation are selected. Then we randomly select cloudless pixels with sun-pixel angles ranging from the smallest angle possible to the maximum in 1° steps. This procedure allows finding possible differences in the relationship between cloudless pixels RBR values and the angle formed with the sun. Sampling a large amount of random pixels allows minimizing the effect of outliers affecting the searched relationship. For the selected pixels, we use Eq. (1) to obtain T_s and T_i. Fig. 5 illustrates the scatterplot of intercept (T_i) vs. the sun-pixel-angle (A) for each cloudless pixel. In this figure, different colors represent different image sequences captured. It can be seen that in spite of the spreading there is an evident relationship between T_i and A. Considering all the images together, we can characterize this dependency with a 4th-degree polynomial function (dashed black line in Fig. 5):

$$T_i = I_4 * A^4 + I_3 * A^3 + I_2 * A^2 + I_1 * A + I_0 \qquad (2)$$

where I_0 to I_4 are the coefficients of the 4th-degree polynomial function.

This dependency shows that for pixels forming a small angle with the Sun, the intercept in Eq. (1) (T_i) is larger and decreases drastically when we move away from the sun position. It has a less pronounced decrease for mid-angle pixels. For pixels away from the sun and close to the horizon (larger angles), T_i increases again due to the horizon brightening effect. On the other hand, T_s does not have any dependency with the distance to the sun, so a mean value can be used.

According to our analyses of the cloudless pixels, a different threshold (T) to each pixel of the image can be applied to the RBR. This threshold will depend on the B
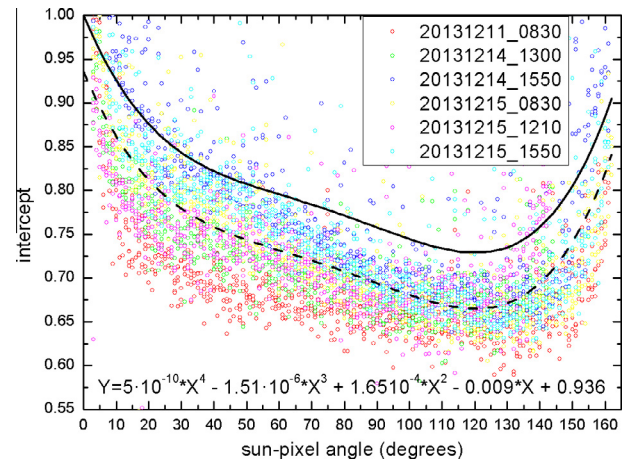

Fig. 5. Dependency of Eq. (1) intercept with the sun-pixel angle. A total of 6 images (in different colors) are plotted. Dashed line is the fourth-degree polynomial fit of the scatter plot. Solid line is the fit with the intercept shifted to 1. Legend indicates the date and time of the images. (For interpretation of the references to colour in this figure legend, the reader is referred to the web version of this article.)

counts for that pixel (related to the amount of light registered by the sensor) and the distance of the pixel to the solar position. In this way, we can use Eq. (1), with T_i calculated applying Eq. (2) to determine the appropriate threshold in each case. It is interesting to note that Eq. (1) characterizes the RBR values for cloudless pixels, therefore, the appropriate threshold for classifying pixels in cloudless and cloudy ones needs to be above T but close enough to minimize misclassifications. Thus we need to apply an offset to T_i. Considering that at solar position ($A = 0$) T_i is equal to 1, i.e. forcing I_0 to 1 in Eq. (2), the new function characterize the upper limit of the scatter plot (solid line in Fig. 5). The final equation for the threshold (T) is

$$T = T_s * B + (I_4 * A^4 + I_3 * A^3 + I_2 * A^2 + I_1 * A + 1) \qquad (3)$$

where T_s and I_1 to I_4 are parameter calculated using Eqs. (1) and (2) to a set of clear-sky cases and characterize a specific sky imager.

3.3. Final algorithm

The two steps described above are combined for the final algorithm. Each sky imager has a different response due to the differences in the sensor and parameters such as the color gain and gamma correction. If these parameters are kept constant, the sky imager can be characterized by fitting Eqs. (1) and (2) for a set of selected sky images with clear-sky conditions. The coefficients that characterize the sky imager are T_s, and I_1 to I_4. The image sequence in Fig. 5 is used for the calculation of the different coefficients. This calibration must be done once, unless internal parameters of the sky imager change. Then, during operation, we follow the next steps:

- Acquisition of the sequence of multi-exposure images.
- Calculate the sun position in the image and the sun-pixel angle for each pixel.
- For each image in the sequence:
– Mask values out of the range of application (85–240 counts on the *B* channel).
– Calculate *T* applying Eq. (3) with the corresponding sky imager coefficients.
– Mark as cloudy every pixel above *T* and as clear-sky the rest of pixels.
- We finally have a sequence of result images with parts of them classified as cloudy or clear-sky (the rest is masked out since is out of the range of application). Several images may have the same pixels classified (more than one image have a specific pixel in the range of application) so the final result is a single image that merges the information from all this multi-exposure result images. The result images should have the same result for a given pixel, but in case of a discrepancy due to outliers, the classification for that pixel is based on the most frequent classification.
- Our sky imager has a shadow band that protects the sensor from the direct sunlight. The shadow band and objects obstructing the image are removed by interpolation yielding a complete picture of the sky dome. The interpolation is made by an iterative procedure that fills the masked areas with the median value of surrounding valid pixels.

3.4. Modeled direct normal irradiance

The methodology explained above allows discriminating the solar obstruction by clouds accurately. In order to validate the methodology, firstly we derived the direct horizontal irradiance (DHI) from the Global Horizontal Irradiance (GHI) and diffuse irradiance (DIF) as DHI = GHI – DIF.

Secondly, using the period comprising between 20 December 2013 to 15 January 2013 and selecting periods of time with unobstructed solar disc (manually checked by visual inspection of the images and the DNI), we formulated an empirical model that estimates DNI values based on the solar zenith angle (θ). In this sense, we observed an exponential dependency between the DHI and the solar zenith angle (Fig. 6) which can be fitted by the following expression:

$$\frac{\text{DHI}}{I_{sc}E_0} = (-0.76 + 0.73 \cdot e^{0.79 \cdot \cos(\theta)}) \qquad (4)$$

where I_{sc} is the solar constant and E_0 is the eccentricity factor. Finally, by means of this dependency and converting the DHI into DNI (DNI = DHI/cos(θ)) our empirical model follows the equation:

$$\text{DNI} = \frac{I_{sc}E_0(-0.76 + 0.73 \cdot e^{0.79 \cdot \cos(\theta)})}{\cos(\theta)} \qquad (5)$$

This model is used to calculate the relative difference between the measured DNI and the modeled one. This relative difference is used to confirm that the solar disk is
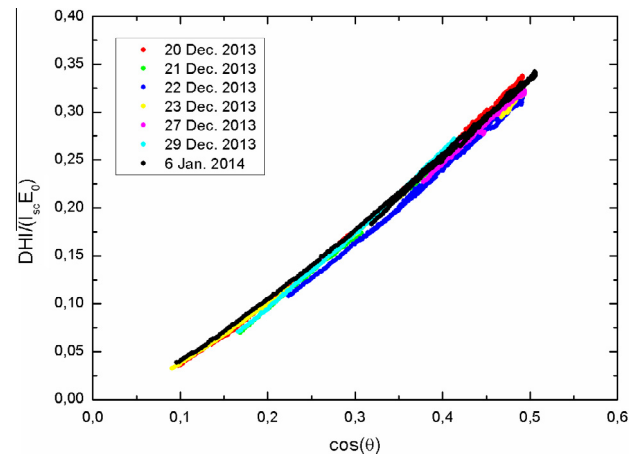

Fig. 6. Dependency of the direct horizontal irradiance and the cosine of the solar zenith angle for clear-sky conditions.

obstructed by clouds. However, this relative difference between the model and the measured DNI during cloud-free conditions is about 12%. This would be the uncertainty of the model, i.e. a reduction of 12% of the DNI or more could be considered as cloud obstructing the solar disk. In order to minimize this difference for a given day, we calculated the daily mean relative difference between the model and the calculated DNI for period of unobstructed sun. Then, that relative difference is added or subtracted to the model for that day. This way we account for factors that are not included in the model such as the aerosol load. In days with no unobstructed solar disk periods, the modeled DNI is applied. Thus, the relative difference between the measured and modeled DNI is reduced to 7%, and we consider this the uncertainty in the detection of unobstructed solar disk.

The modeled DNI, modified based on the sky conditions, is used to quantify the accuracy of our detection method. Cases with a difference smaller than the uncertainty of the model are considered as cloud-free sky in the sun position, and cases with a difference greater than the uncertainty of the model are considered to have the sun obstructed by clouds.

4. Results

We applied the multi-exposure adaptive threshold technique during the period of time between 20 December 2013 and 15 January 2014. All images were captured every 5 min when the sun elevation is above 15° every day with a few gaps due to problems with the computer or the network connection. Firstly, a study case with a great variety of cloud coverage and sun obstruction is analyzed in detail in Section 4.1 and, subsequently, statistical results based on the proposed model are shown in Section 4.2.

4.1. A case study

We analyzed in detail the images during 21 December 2013. This day contains a variety of situations that allows

us to illustrate our methodology. Early in the morning the day is completely cloud-free. Around 08:45 GMT clouds start to develop and move from the north-east. Close to 09:30 GMT the sky dome is practically covered by clouds. However, the sun remains unobstructed most of the time. Clouds dissipation starts around 10:00 GMT and the sky remains cloud-free until later in the afternoon when, about 14:30 GMT some clouds develop in the south–west, close to the sun position at that time. Fig. 7 shows the GHI, DIF and DNI during the selected day. Early in the morning, DIF and GHI increases, indicating the presence of clouds but with the sun unobstructed. About 9:35 GMT there is a sudden decrease of the GHI and the DNI, pointing out the presence of a cloud obstructing the sun position. The completely cloud-free sky period is observed with the smoothness of the GHI and small values of DIF. Finally, in the afternoon another cloud passing through the sun position can be observed by looking at the sudden decrease of the DNI. Markers in Fig. 7 indicate times when we look at the cloud detection images.

Fig. 8 shows the sequence of images at the times specified on Fig. 7. The first column is the original single exposure image. The second column is the result of applying the RBR to the first column and column 3 shows the result applying the threshold technique to the multi-exposure sequence as explained in the previous section. Column 2 and 3 have the sun position marked in black if the algorithm detected that position as cloudy and red if it was detected as clear-sky.

We observe that, during the morning, the new algorithm detects correctly that the sun is unobstructed by clouds and also detects the clouds pass in front of the sun position. The images corresponding with the evening also show the good performance of the new algorithm, detecting clouds around the sun position. The images on row 3 (12:00) also show the good performance of the new algorithm on completely cloud-free situations.

Fig. 8. Sequence of images during 21 December 2013. First column is the original single exposure image. The second column is the result applying the red-to-blue ratio to the first column. Column 3 shows the result applying the threshold technique to the multi-exposure sequence. Columns 2 and 3 have the sun position marked as black if the algorithm classified the sun position as cloudy and red if it was classified as clear-sky. (For interpretation of the references to color in this figure legend, the reader is referred to the web version of this article.)

4.2. Statistical analysis

A validation of the method can be performed by a statistical analysis of the goodness of the detection of clouds in the sun position. For time coincident cases with images (every 5 min) and DNI data, we separated cases where the algorithm indicates that the sun is obstructed by clouds and those cases classified as cloud-free in the sun position. For each case, we calculated the relative difference (in percentage) between the calculated and modeled DNI. Hence, two frequency histograms are built with the percent of reduction of DNI (respect to the model) for cases with sun obstructed/unobstructed by clouds. The histogram for unobstructed sun cases is shown in Fig. 9a. We observe that about 78% of cases classified as clear sun path have a reduction of the DNI with respect to the modeled values smaller or equal to 7% (model uncertainty),considering these cases as well classified. The remaining 22% are
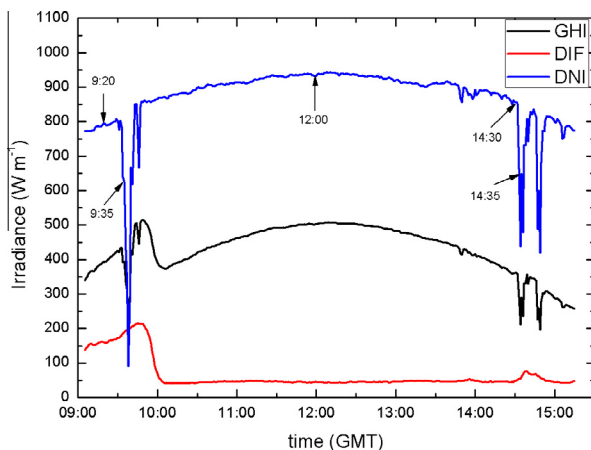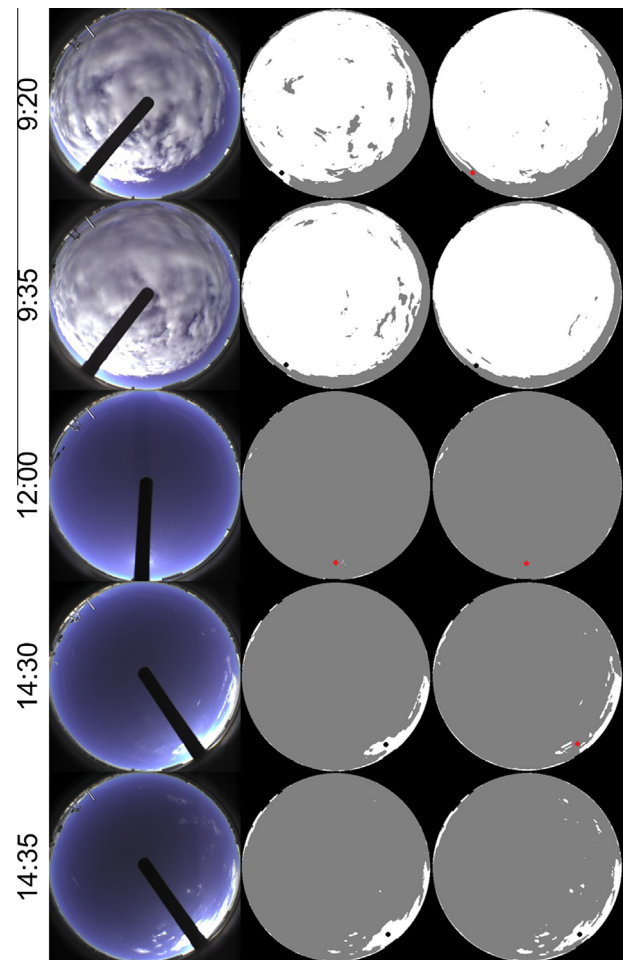

Fig. 7. Global Horizontal Irradiance (GHI), diffuse irradiance (DIF) and direct normal irradiance (DNI) during 21 December 2013. Specific times with coincident sky images are marked with arrows.
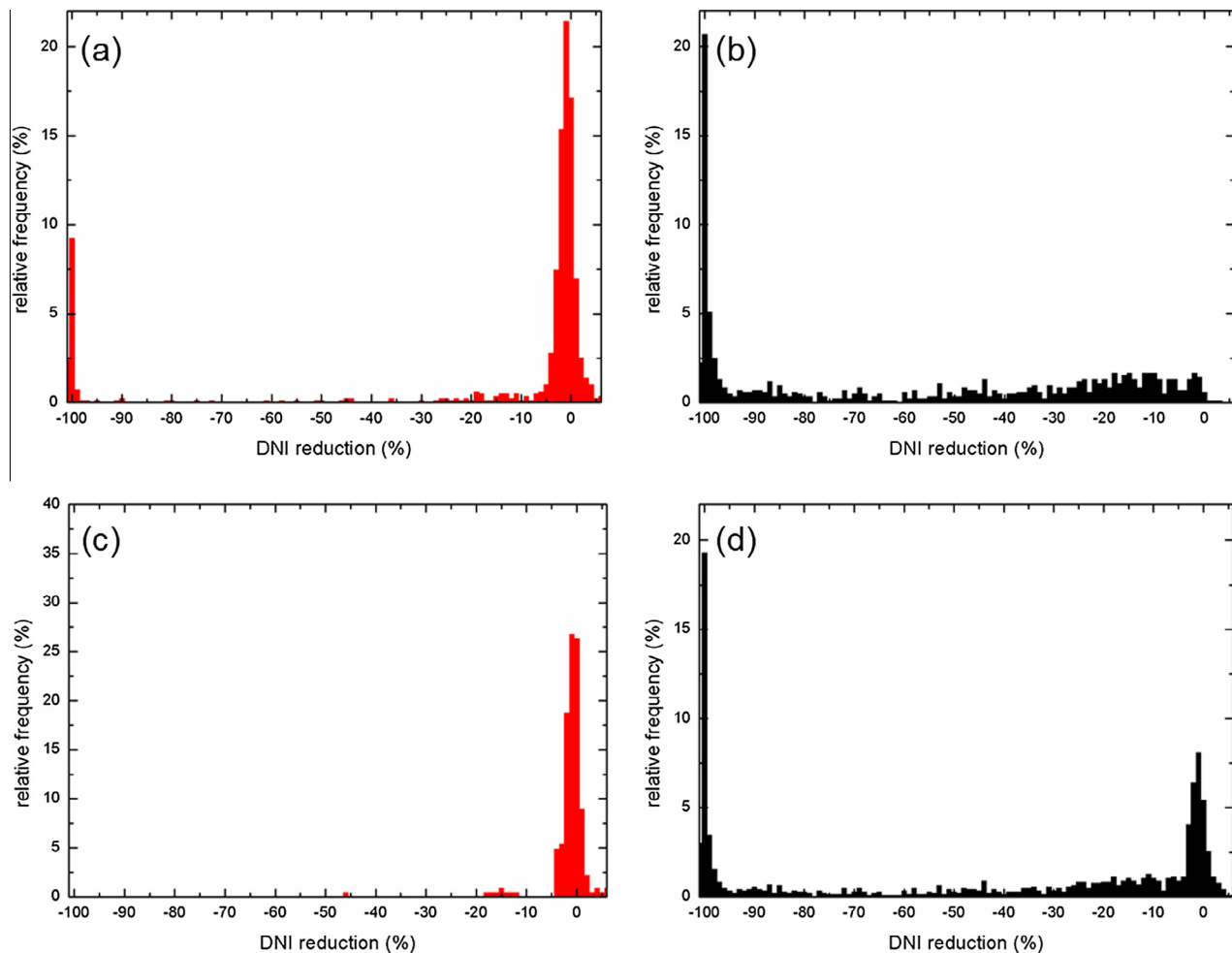
Fig. 9. Relative frequency histograms of the direct normal irradiance reduction respect to the model for cases classified as sun unobstructed (left panels), and cases classified as sun obstructed (right panels). Top panels show results with the multi-exposure adaptive technique and bottom panels show results with the red-to-blue ration threshold technique. (For interpretation of the references to color in this figure legend, the reader is referred to the web version of this article.)

misclassified, with reductions of the DNI until 100%. We would like to highlight that 13% of the cases show reductions of the DNI between 95% and 100%, corresponding to overcast conditions, some of them with rain. If we exclude them from the analysis (they are not relevant in solar technology applications), we have a misclassification of about 9% of the cases. Finally, the histogram shown in Fig. 9b reveals that about 90% of the data with reductions of 7% or more are classified by the algorithm as sun obstructed by clouds.

During the same period, images captures with a single exposure time were analyzed using the red-to blue ratio threshold technique. The same interpolation process was used to remove the shadow band. Using the same statistical analysis, we observe that about 95% of cases classified as clear sun path, have a reduction of the DNI with respect to the modeled values smaller or equal to model uncertainty (Fig. 9c), yielding to a misclassification of about 5%. On the other hand, 67% of the cases with reductions of the DNI greater than 7% are classified as cloudy by the classical RBR method as sun obstructed by clouds (Fig. 9d).

This shows that on clear-sky conditions the classical method misclassifies about 33% of the cases and the new method misclassifies about 9% of the cases.

5. Conclusions

The methodology presented in this work results on a robust way to detect clouds in sky imagers without the limitation of single exposure images where parts of the sky are saturated. We evaluated the ability of this method to detect clouds in the sun position since this is one of the main concerns in solar energy technologies applications. The procedure has been tested on a CCD sensor sky imager with shadow band, which introduces an additional source of error because the shadow band needs to be eliminated by interpolation.

A case study analysis reveals that the method classifies the entire image accurately, and the classification of clear-sky and cloudy pixels is similar to what the human eye sees in the images. The statistical analysis shows that the method works well for most conditions although it

presents some limitations for overcast and rainy conditions. During these cases, the images present a blue cast due to the color balance the sky imager applies, causing clouds to appear bluish instead of grey in the images. This makes the cloud to be below the RBR threshold for pixels close to the sun where the threshold takes higher values. In any case, focusing on solar technology applications, these misclassifications are not a problem since the power plants do not operate in these situations and they can be excluded of the analysis.

Comparing the classification rate of the new method and the classical RBR of a single exposure time image, we observe that conditions with the sun unobstructed by clouds (DNI reductions smaller than 7%) are misclassified on 9% of the cases with the new method and on 33% of the cases with the classic RBR method. This shows that, when the sun is unobstructed by clouds, misclassification with the new method is smaller. The main problem with sky imagers is that the circumsolar area is classified as cloudy in numerous situations, but with this new method, we are discriminating more accurately clear-sky conditions as they are better classified (up to 24%). This is essential if the cloud information derived from sky imagers needs to be used in solar technologies for forecast model.

This methodology can be applied to other sky imagers easily as long as the sky imager parameters are kept constant, including sky imagers without a shadow band, where it is expected to provide better classification rates since the interpolation process is not necessary. Also, the control of the color balance of the imager is expected to remove the blue cast that overcast images present, solving the misclassification in these situations.

Acknowledgements

References

Ahmad, M.J., Tiwari, G.N., 2011. Solar radiation models – a review. Int. J. Energy Res. 35, 271–290.

Antón, M., Gil, J.E., Cazorla, A., Fernández-Gálvez, J., Foyo-Moreno, I., Olmo, F.J., Alados-Arboledas, L., 2011. Short-term variability of experimental ultraviolet and total solar irradiance in Southeastern Spain. Atmos. Environ. 45, 4815–4821. http://dx.doi.org/10.1016/j.atmosenv.2011.06.020.

Calbó, J., Sabburg, J., 2008. Feature extraction from whole-sky ground-based images for cloud-type recognition. J. Atmos. Ocean. Technol. 25, 3–14.

Cazorla, A., Olmo, F.J., Alados-Arboledas, L., 2008. Using a sky imager for aerosol characterization. Atmos. Environ. 42, 2739–2745.

Chow, C.W., Urquhart, B., Dominguez, A., Kleissl, J., Shields, J., Washom, B., 2011. Intra-hour forecasting with a total sky imager at the UC San Diego solar energy testbed. Sol. Energy 85, 2881–2893.

Crispim, E.M., Ferreira, P.M., Ruano, A.E., 2008. Prediction of the solar radiation evolution using computational intelligence techniques and cloudiness indices. Int. J. Innovative Comput. Inform. Contr. 4 (5), 1121–1133.

Debevec, P. Malik, J.1997. Recovering high dynamic range radiance maps from photographs. In: Proceedings of the ACM SIGGRAPH'97, Los Angeles CA, 369–378.

Eck, M., Hirsch, T., 2007. Dynamics and control of parabolic trough collector loops with direct steam generation. Sol. Energy 81, 268–279.

Ghonima, M.S., Urquhart, B., Chow, C.W., Shields, J.E., Cazorla, A., Kleissl, J., 2012. A method for cloud detection and opacity classification based on ground based sky imagery. Atmos. Meas. Tech. 5, 2881–2892. http://dx.doi.org/10.5194/amt-5-2881-2012.

González, Y., Lopez, C., Cuevas, E. Automatic observation of cloudiness: analysis of allsky images, TECO-2012, In: WMO Technical Conference on Meteorological and Environmental Instruments and Methods of Observation, Brussels, Belgium, 16–18 October 2012.

Hammer, A., Heinemann, D., Hoyer, C., Kuhlemann, R., Lorenz, E., Muller, R., Beyer, H., 2003. Solar energy assessment using remote sensing technologies. Remote Sens. Environ. 86, 423–432.

Johnson, R., Hering, W., Shields, J., 1989. Automated visibility and cloud cover measurements with a solid-state imaging system. Tech. Rep., University of California, San Diego, Scripps Institution of Oceanography, Marine Physical Laboratory, SIO Ref. 89–7, GL-TR- 89–0061, 128 pp.

Kazantzidis, A., Tzoumanikas, P., Bais, A.F., Fotopoulos, S., Economou, G., 2012. Cloud detection and classification with the use of whole-sky ground-based images. Atmos. Res. 113, 80–88. http://dx.doi.org/10.1016/j.atmosres.2012.05.005.

Kratzenberg, M.G., Beyer, H.G., Colle, S., Albertazzi, A., 2006. Uncertainty calculations in pyranometermeasurements and application. In: Proceedings of the American Society of Mechanical Engineers (ASME). 2006 International Solar Energy Conference (ISEC 2006). July 8–13, 2006, Adam's Mark Hotel, Denver, Colorado, USA.

Long, C.N., Sabburg, J., Calbó, J., Pagès, D., 2006. Retrieving cloud characteristics from ground-based daytime color all-sky images. J. Atmos. Ocean. Technol. 23, 633–652.

Long, C.N., 2010. Correcting for circumsolar and near-horizon errors in sky cover retrievals from sky images. The Open Atmos. Sci. J. 4, 45–52.

Lyamani, H., Olmo, F.J., Alados-Arboledas, L., 2010. Physical and optical properties of aerosols over an urban location in Spain: seasonal and diurnal variability. Atmos. Chem. Phys. 10 (1), 239–254. http://dx.doi.org/10.5194/acp-10-239-2010.

Marquez, R., Coimbra, C.F.M., 2013. Intra-hour DNI forecasting based on cloud tracking image analysis. Sol. Energy 91, 327–336.

Marquez, R., Gueorguiev, V.G., Coimbra, C.F.M., 2013. Forecasting solar irradiance using sky cover índices. J. Solar Energy Eng. Trans. ASME 135, 011017.

Medrano, M., Gil, A., Martorell, I., Potau, X., Cabeza, L.F., 2010. State of the art on high-temperature thermal energy storage for power generation. Part 2 – Case studies. Renew. Sustain. Energy Rev. 14, 56–72.

Pfister, G., McKenzie, R.L., Liley, J.B., Thomas, A., Forgan, B.W., Long, C.N., 2003. Cloud coverage based on all-sky imaging and its impact on surface solar irradiance. J. Appl. Meteorol. 42, 1421–1434.

Sharma, A., Tyagi, V.V., Chen, C.R., Buddhi, D., 2009. Review on thermal energy storage with phase change materials and applications. Renew. Sustain. Energy Rev. 13, 318–345.

Shields, J., Johnson, R., Karr, M., Wertz, J., 1998. Automated day/night whole sky imagers for field assessment of cloud cover distributions and radiance distributions. In: Tenth Symposium on Meteorological Obser-Vations and Instrumentation. American Meteorological Society.

Shields, J., Karr, M., Burden, A., Johnson, R., Mikuls, V., Streeter, J., Hodgkiss, W., 2009. Research toward multi-site characterization of sky obscuration by clouds. Marine Physical Laboratory. In: Scripps Institution of Oceanography, University of California San Diego, Technical Note 274.

Souza-Echer, M.P., Pereira, E.B., Bins, L.S., Andrade, M.A.R., 2006. A simple method for the assessment of the cloud cover state in high-latitude regions by a ground-based digital camera. J. Atmos. Ocean. Technol. 23, 437–447.

Tapakis, R., Charalambides, A.G., 2013. Equipment and methodologies for cloud detection and classification: a review. Sol. Energy 95, 392–430. http://dx.doi.org/10.1016/j.solener.2012.11.015.

Tomson, T., Tamm, G., 2006. Short-term variability of solar radiation. Sol. Energy 80, 600–606.

Tomson, T., 2010. Fast dynamic processes of solar radiation. Sol. Energy 84, 318–323.

Tovar, J., Olmo, F.J., Alados-Arboledas, L., 1998. One minute global irradiance probability density distributions conditioned to the optical air mass. Sol. Energy 62 (6), 387–393.

Tovar, J., Olmo, F.J., Batlles, F.J., Alados-Arboledas, L., 1999. One minute kb and kd probability density distributions conditioned to the optical air mass. Sol. Energy 65 (5), 297–304.

Urquhart, B., Kurtz, B., Dahlin, E., Ghonima, M., Shields, J.E., Kleissl, J., 2014. Development of a sky imaging system for short-term solar power forecasting. Atmos. Meas. Tech. Discuss. 7 (20), 4859–4907. http://dx.doi.org/10.5194/amtd-7-4859-2014.

Woyte, A., Belmans, R., Nijs, J., 2007. Fluctuations in instantaneous clearness index: analysis and statistics. Sol. Energy 81, 195–206.